Rapid Filamentation Zones in Intense Tropical Cyclones

CHRISTOPHER M. ROZOFF, WAYNE H. SCHUBERT, AND BRIAN D. MCNOLDY

Department of Atmospheric Science, Colorado State University, Fort Collins, Colorado

JAMES P. KOSSIN

Cooperative Institute for Meteorological Satellite Studies, University of Wisconsin—Madison, Madison, Wisconsin

(Manuscript received 11 November 2003, in final form 12 August 2004)

ABSTRACT

Intense tropical cyclones often possess relatively little convection around their cores. In radar composites, this surrounding region is usually echo-free or contains light stratiform precipitation. While subsidence is typically quite pronounced in this region, it is not the only mechanism suppressing convection. Another possible mechanism leading to weak-echo moats is presented in this paper. The basic idea is that the strain-dominated flow surrounding an intense vortex core creates an unfavorable environment for sustained deep, moist convection. Strain-dominated regions of a tropical cyclone can be distinguished from rotation-dominated regions by the sign of $S_1^2 + S_2^2 - \zeta^2$, where $S_1 = u_x - v_y$ and $S_2 = v_x + u_y$ are the rates of strain and $\zeta = v_x - u_y$ is the relative vorticity. Within the radius of maximum tangential wind, the flow tends to be rotation-dominated ($\zeta^2 > S_1^2 + S_2^2$), so that coherent structures, such as mesovortices, can survive for long periods of time. Outside the radius of maximum tangential wind, the flow tends to be strain-dominated ($S_1^2 + S_2^2 > \zeta^2$), resulting in filaments of anomalous vorticity. In the regions of strain-dominated flow the filamentation time is defined as $\tau_{\text{fil}} = 2(S_1^2 + S_2^2 - \zeta^2)^{-1/2}$. In a tropical cyclone, an approximately 30-km-wide annular region can exist just outside the radius of maximum tangential wind, where τ_{fil} is less than 30 min and even as small as 5 min. This region is defined as the rapid filamentation zone. Since the time scale for deep moist convective overturning is approximately 30 min, deep convection can be significantly distorted and even suppressed in the rapid filamentation zone. A nondivergent barotropic model illustrates the effects of rapid filamentation zones in category 1–5 hurricanes and demonstrates the evolution of such zones during binary vortex interaction and mesovortex formation from a thin annular ring of enhanced vorticity.

1. Introduction

Figures 1a,d show 133- and 123-min composites of the horizontal radar reflectivity for Hurricane Gilbert on 13 and 14 September 1988. On 13 September, Gilbert was at peak intensity with a central minimum sea level pressure (MSLP) reaching 888 hPa. During this time, Gilbert exhibited a compact eyewall between 8 and 20 km from the center. Except for two small spiral rain bands to the northeast of the eyewall, convective cells were absent between radii of 20 and 68 km. Although convection was sparse, there was widespread, but light stratiform precipitation. On 14 September, Gilbert's MSLP rose slightly to 895 hPa, corresponding to an eyewall replacement cycle. The inner eyewall was between 8- and 20-km radius and the newly formed outer eyewall between 55- and 100-km radius, with a 35-km weak-echo annulus (or moat) between the inner and outer eyewalls. Here, we define a moat as a weak-echo region outside of the primary eyewall of a storm, whereas Simpson and Starrett (1955) referred to a cloud-free region in the eye as a moat. Based on the National Oceanic and Atmospheric Administration (NOAA) WP-3D aircraft flight track described in Black and Willoughby (1992), Figs. 1b,e show the radial profiles of flight-level (700 hPa) tangential wind for 13 and 14 September. On 13 September, the tangential wind maximum was 75–80 m s^{-1} at 10-km radius. By 14 September, the inner tangential wind maximum was 66–69 m s^{-1} at 10-km radius, while the outer tangential wind maximum was 49–52 m s^{-1} at 61–67-km radius. The strong cyclonic circulation was very deep with 50 m s^{-1} winds reaching a height of 12 km.

Weak-echo moats, such as the one shown in Fig. 1,

Corresponding author address: Christopher M. Rozoff, Colorado State University, Fort Collins, CO 80523-1371.
E-mail: rozoff@atmos.colostate.edu

© 2006 American Meteorological Society

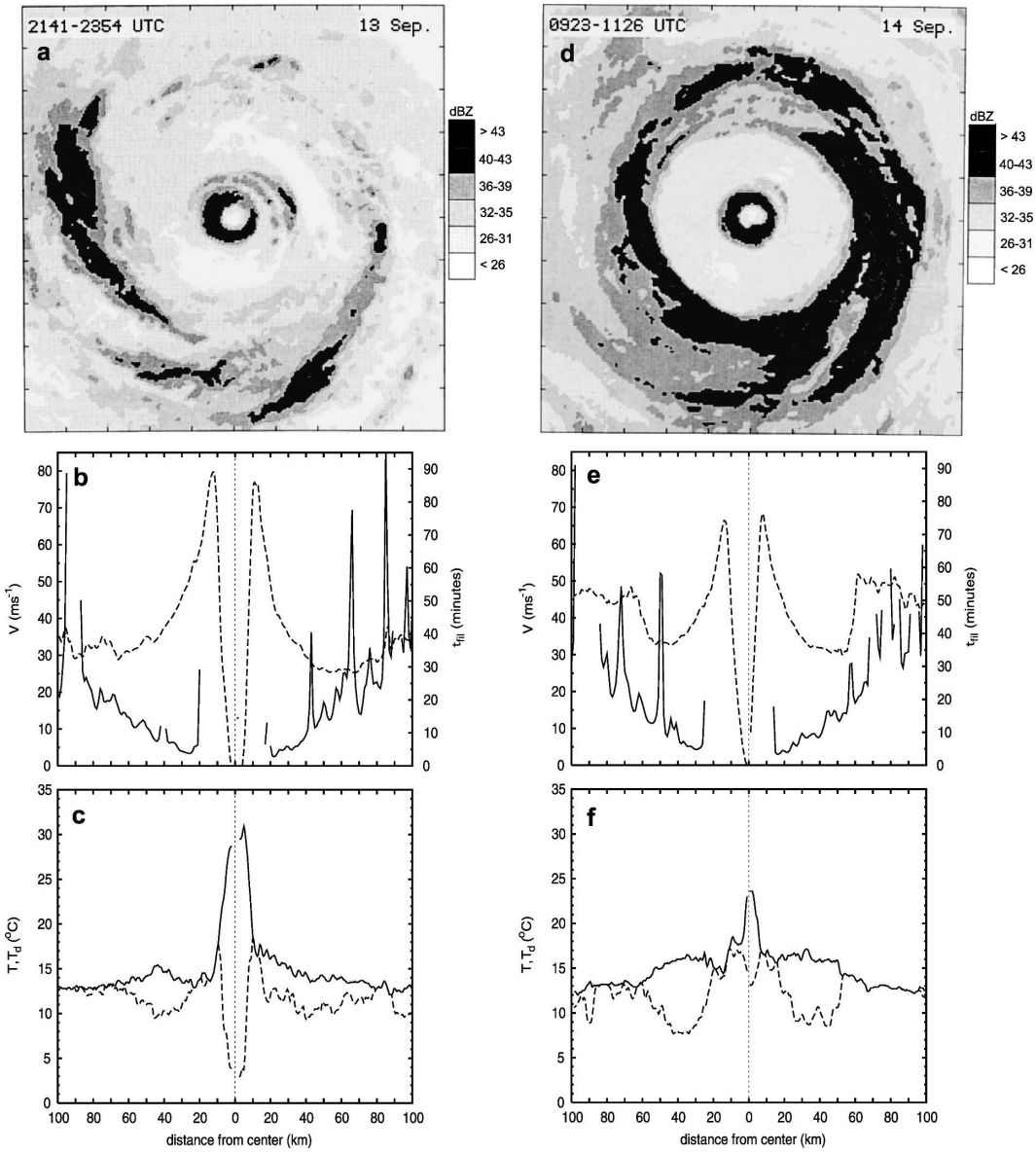

FIG. 1. Composite horizontal radar reflectivity of Hurricane Gilbert for (a) 2141–2354 UTC 13 Sep 1988 and (d) 0923–1126 UTC 14 Sep 1988. The domain is 240 km × 240 km, with tick marks every 24 km. Also, flight-level tangential wind (dashed line) and filamentation time, as computed from (11), for the 700-hPa flights for (b) 13 and (e) 14 Sep; corresponding temperature and dewpoint temperature along the same flight track on (c) 13 and (f) 14 Sep. Detailed descriptions of Hurricane Gilbert are given by Black and Willoughby (1992), Samsury and Zipser (1995), and Dodge et al. (1999).

are often found in intense tropical cyclones (TCs). The tendency for convection to be suppressed in the moat region is generally attributed to mesoscale subsidence between two regions of strong upward motion. According to Dodge et al. (1999), there appears to be lower tropospheric subsidence in the moat, but the upper tropospheric vertical motion is apparently upward. Through analysis of Doppler radar data, Dodge et al. found that the moat of Hurricane Gilbert was characterized by weak stratiform precipitation with 0.5–1.0 m s^{-1} downward motion below the bright band observed near 5-km height, and 0.5 m s^{-1} upward motion above 5 km. Evidence that subsidence plays a role in the formation of moats is presented in Figs. 1c,f. These figures show the flight-level temperature and dewpoint temperature for radial legs across the storm. On 13 September, the dewpoint depressions in the moat reached 5°C. On 14 September, the dewpoint depres-

sions in the moat were approximately 8°C, nearly as large as in the eye, which is a telltale sign of subsidence in the moat. With larger dewpoint depressions occurring on the second day, it is likely that the secondary circulation associated with the secondary eyewall, additive to the primary eyewall secondary circulation, was enhancing subsidence and dewpoint depressions in the moat.

The above observations of Hurricane Gilbert suggest that lower tropospheric subsidence plays an important role in the dynamics of the moat. However, there are additional dynamics at work. In the present paper, the moat is determined to be a region of strain-dominated flow in which essentially all fields are filamented. The concept of strong strain-dominated regions outside of primary eyewalls is not a new one. For example, in analogy with terminology used to describe the surroundings of the stratospheric polar vortex, Guinn and Schubert (1993) refer to the region outside the hurricane's high potential vorticity (PV) core as the surf zone, a zone where differential rotation causes PV wave breaking to occur repeatedly. In addition, Shapiro and Montgomery (1993) allude to such processes in developing their asymmetric balance model, while Kossin et al. (2000) also provide a qualitative description of such straining zones and hypothesize that such zones are possible reasons for the weak-echo moat. The present paper explores these ideas in greater detail. In section 2, strong straining zones around vortex cores are discussed in the context of barotropic dynamics, and the concept of a rapid filamentation zone is introduced. In section 3 we use numerical results from a barotropic model to explore the necessary conditions for forming moats around eyewalls. The barotropic model is initialized with various eyewall vorticity distributions embedded within a "stirred" field of net cyclonic vorticity. In sections 4 and 5 we illustrate the evolution of rapid filamentation zones during binary vortex interaction and mesovortex formation. Finally, a summary of the results and conclusions is presented in section 6.

2. Basic concepts

In Cartesian coordinates, the equations for the *f*-plane, nondivergent, barotropic model are

$$\frac{\partial \zeta}{\partial t} + \frac{\partial(\psi, \zeta)}{\partial(x, y)} = \nu \nabla^2 \zeta, \tag{1}$$

and

$$\zeta = \nabla^2 \psi, \tag{2}$$

where ζ is the relative vorticity, $\partial(\cdot, \cdot)/\partial(x, y)$ is the Jacobian operator, ψ is the streamfunction for the nondivergent flow $(u, v) = (-\partial\psi/\partial y, \partial\psi/\partial x)$, and ν is the constant coefficient of viscosity.

To better understand the dynamics of the rapid filamentation zone, we refer to the equation governing the evolution of the vorticity gradient (Okubo 1970; Weiss 1991; Brachet et al. 1988). Temporarily neglecting diffusion and computing $\partial(1)/\partial x \pm i\partial(1)/\partial y$, we obtain

$$\frac{D}{Dt}\begin{pmatrix} \zeta_x + i\zeta_y \\ \zeta_x - i\zeta_y \end{pmatrix} = \begin{pmatrix} \frac{1}{2} i\zeta & -\frac{1}{2}(S_1 + iS_2) \\ -\frac{1}{2}(S_1 - iS_2) & -\frac{1}{2} i\zeta \end{pmatrix} \times \begin{pmatrix} \zeta_x + i\zeta_y \\ \zeta_x - i\zeta_y \end{pmatrix}, \tag{3}$$

where

$$S_1 = \frac{\partial u}{\partial x} - \frac{\partial v}{\partial y} \quad \text{and} \quad S_2 = \frac{\partial v}{\partial x} + \frac{\partial u}{\partial y} \tag{4}$$

are the rates of strain and $(D/Dt) = (\partial/\partial t) + u(\partial/\partial x) + v(\partial/\partial y)$ is the material derivative. In the meteorological literature, $\frac{1}{2}S_1$ is referred to as the stretching deformation, $\frac{1}{2}S_2$ as the shearing deformation, and $\frac{1}{2}(S_1^2 + S_2^2)^{1/2}$ as the total deformation. Values of S_1 and S_2 are dependent on the orientation of the coordinate axes, but the value of $(S_1^2 + S_2^2)^{1/2}$ is not.

The eigenvalues of the 2×2 matrix on the right-hand side of (3) are given by $\pm\frac{1}{2}i(\zeta^2 - S_1^2 - S_2^2)^{1/2}$ if $\zeta^2 > S_1^2 + S_2^2$ (rotation dominated), or by $\pm\frac{1}{2}(S_1^2 + S_2^2 - \zeta^2)^{1/2}$ if $S_1^2 + S_2^2 > \zeta^2$ (strain dominated). In many TC situations, $S_1^2 + S_2^2$ and ζ^2 can be considered nearly constant along a trajectory, because the azimuthal wind is much larger than the radial wind and the flow is nearly axisymmetric, resulting in particle trajectories that are nearly circular. When the eigenvalues are almost constant along a trajectory, the solutions of (3) are approximated by linear combinations of

$$\exp\left[\pm\frac{1}{2} i(\zeta^2 - S_1^2 - S_2^2)^{1/2} t\right] \quad \text{if} \quad \zeta^2 > S_1^2 + S_2^2 \tag{5}$$

or

$$\exp\left[\pm\frac{1}{2}(S_1^2 + S_2^2 - \zeta^2)^{1/2} t\right] \quad \text{if} \quad S_1^2 + S_2^2 > \zeta^2. \tag{6}$$

Because the solutions given in (5) are oscillatory, coherent structures survive in regions where vorticity dominates strain. In contrast, the solutions given in (6) are exponential, so that regions where strain dominates vorticity are characterized by vorticity-gradient sheets.

These vorticity-gradient sheets are long, thin layers across which vorticity rapidly changes. In the strain-dominated regions, we define the filamentation time $\tau_{\text{fil}}(x, y)$ as

$$\tau_{\text{fil}} = 2(S_1^2 + S_2^2 - \zeta^2)^{-1/2} \quad \text{for} \quad S_1^2 + S_2^2 > \zeta^2. \quad (7)$$

Our primary hypothesis is that cumulonimbus convection becomes highly distorted, and even suppressed, in regions where the filamentation time τ_{fil} is less than τ_{conv}—the time scale for deep, moist convective overturning. It can be argued that τ_{conv} should be taken as the time required for a parcel to travel from the top of the boundary layer (600 m) to the anvil level (15 km) at a typical cumulonimbus updraft velocity of 8 m s^{-1}; namely, $\tau_{\text{conv}} = 14.4$ km/8 m s^{-1} = 30 min. It can also be argued that hurricane convective cells have weaker updraft speeds (3–4 m s^{-1}), but only extend slightly above the freezing level before merging into the general mesoscale rising motion. This argument, with its weaker updrafts and smaller vertical depths, also leads to estimates of τ_{conv} near 30 min. With some subjectivity in the estimate of τ_{conv}, a rapid filamentation zone is operationally defined as a region in which $\tau_{\text{fil}} < \tau_{\text{conv}} = 30$ min.

To estimate filamentation times for TCs, it is useful to express $S_1^2 + S_2^2 - \zeta^2$ in polar coordinates. Thus, transforming to the polar coordinates (r, θ), we obtain

$$S_1^2 + S_2^2 = \left(\frac{\partial v_r}{\partial r} - \frac{v_r}{r} - \frac{\partial v_\theta}{r\partial\theta}\right)^2 + \left(\frac{\partial v_\theta}{\partial r} - \frac{v_\theta}{r} + \frac{\partial v_r}{r\partial\theta}\right)^2, \quad (8)$$

and

$$\zeta^2 = \left(\frac{\partial v_\theta}{\partial r} + \frac{v_\theta}{r} - \frac{\partial v_r}{r\partial\theta}\right)^2, \quad (9)$$

where v_r and v_θ denote the radial and azimuthal components of velocity, respectively. In the special case of axisymmetry with no radial flow, (8) and (9) yield

$$\frac{1}{4}(S_1^2 + S_2^2 - \zeta^2) = -\frac{v_\theta}{r}\frac{\partial v_\theta}{\partial r} = -\omega\left(\omega + r\frac{\partial\omega}{\partial r}\right), \quad (10)$$

where $\omega = v_\theta/r$ is the angular velocity. Using (10) in (7) we obtain the following for the axisymmetric case:

$$\tau_{\text{fil}} = \left(-\frac{v_\theta}{r}\frac{\partial v_\theta}{\partial r}\right)^{-1/2} = \left[-\omega\left(\omega + r\frac{\partial\omega}{\partial r}\right)\right]^{-1/2} \quad \text{for} \quad \frac{v_\theta}{r}\frac{\partial v_\theta}{\partial r} < 0. \quad (11)$$

To gain insight into the spatial distribution of τ_{fil}, we now consider three simple examples. The first example is the Rankine vortex. Its angular velocity is defined as

$$\omega(r) = \omega_0\begin{cases} 1 & \text{if} \quad 0 \le r < a \\ (a/r)^2 & \text{if} \quad a \le r < \infty, \end{cases} \quad (12)$$

where a is the radius of maximum tangential wind and ω_0 is the constant angular velocity inside $r = a$. Using (12) in (10) we obtain

$$\frac{1}{4}(S_1^2 + S_2^2 - \zeta^2) = \omega_0^2\begin{cases} -1 & \text{if} \quad 0 \le r < a \\ (a/r)^4 & \text{if} \quad a < r < \infty, \end{cases} \quad (13)$$

which shows that there is an abrupt change from vorticity-dominated flow inside $r = a$ to strain-dominated flow outside $r = a$. In the strain-dominated region, the filamentation time as defined in (11) is

$$\tau_{\text{fil}}(r) = \omega_0^{-1}(r/a)^2 \quad \text{for} \quad a < r < \infty. \quad (14)$$

For $a = 15$ km and $\omega_0^{-1} = (50 \text{ m s}^{-1}/15 \text{ km})^{-1} = 300$ s, the filamentation time $\tau_{\text{fil}}(r)$ varies from 5 min at $r = 15$ km to 60 min at $r = 52$ km and the rapid filamentation zone is the annular region defined by 15 km $< r <$ 37 km.

To help understand when rapid filamentation zones first appear and how they evolve during the TC life cycle, we now consider a family of Gaussian vortices with the tangential wind profile

$$v_\theta(r) = \frac{\Gamma}{2\pi r}(1 - e^{-r^2/b^2}), \quad (15)$$

where the constant Γ is the circulation at large radii and b is the e-folding distance of the vorticity distribution. The maximum tangential wind occurs at $r_{\max} \approx 1.121b$ and has the value $v_\theta(r_{\max}) \approx 0.638\ \Gamma/(2\pi b)$. The vorticity distribution associated with (15) is $\zeta(r) = [\Gamma/(\pi b^2)]$ $\exp(-r^2/b^2)$ and the filamentation time, found by using (15) in (11), is

$$\tau_{\text{fil}}(r) = \frac{2\pi b^2}{\Gamma}\left(\frac{r}{b}\right)^2(1 - e^{-r^2/b^2})^{-1/2} \times \left[1 - \left(1 + \frac{2r^2}{b^2}\right)e^{-r^2/b^2}\right]^{-1/2} \quad \text{for} \quad \frac{\partial v_\theta}{\partial r} < 0. \quad (16)$$

With the choice $\Gamma/(2\pi) = 7.5 \times 10^5$ m^2 s^{-1}, Fig. 2 illustrates $v_\theta(r)$ and $\tau_{\text{fil}}(r)$ for various values of b. The values of b represent a tropical storm ($b = 20$ km) and category 1–5 (Saffir–Simpson scale) TCs (i.e., $b = 13.0$, 10.2, 8.5, 7.4, 6.3 km, respectively). Decreasing b in-

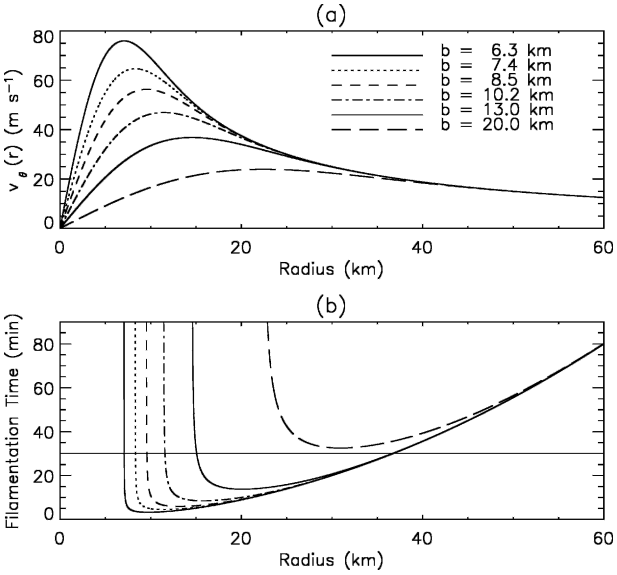

FIG. 2. (a) Radial profiles of v_θ (r) as given by (15) for six different values of the parameter b. (b) Corresponding radial profiles of $\tau_{\text{fil}}(r)$ as given by (16). The filamentation times $\tau_{\text{fil}}(r)$ are plotted only in the strain-dominated regions, where $S_1^2 + S_2^2 - \zeta^2 > 0$.

creases the maximum tangential wind and decreases the radius of maximum wind. The sequence of curves in Fig. 2 can be interpreted as typical profiles that occur during the intensification from a tropical storm to a category 5 TC. The filamentation times shown in Fig. 2b are defined in the region where $\partial v_\theta/\partial r < 0$. As r approaches the radius of maximum wind from the right, the filamentation time approaches infinity for each value of b. As r increases, all curves asymptotically approach each other and increase as r^2 [i.e., with the same far-field behavior as the Rankine vortex (14)]. The $\tau_{\text{fil}}(r)$ curve for the tropical storm lies above τ_{conv}. However, as the idealized Gaussian cyclone becomes stronger, the filamentation time scale dips well below τ_{conv} and the region affected by such strain-dominated flow grows. In the rapid filamentation zone, patches of anomalous vorticity are expected to be quickly filamented into arbitrarily thin strips, which are ultimately lost to diffusion.

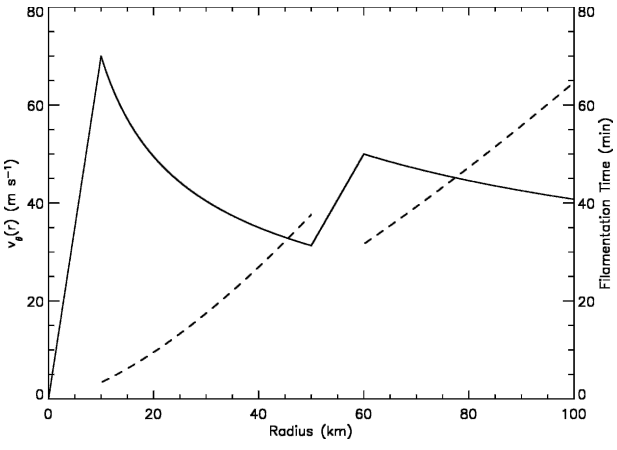

FIG. 3. An idealized vortex with a secondary eyewall. The solid curve is v_θ (r) as given by (17), and the dashed curve is the filamentation time $\tau_{\text{fil}}(r)$, as given by (18). The filamentation time is plotted only in the regions, where $S_1^2 + S_2^2 - \zeta^2 > 0$.

To understand how a secondary eyewall can influence the rapid filamentation zone, we consider a third wind profile, which is an idealization of the Hurricane Gilbert wind profile shown in Fig. 1e. The tangential wind for the parameterized concentric eyewall situation is given by

$$v_\theta(r) = \begin{cases} v_1(r/r_1) & \text{if} \quad 0 \le r < r_1 \\ v_1(r_1/r)^{0.5} & \text{if} \quad r_1 \le r < r_2 \\ [v_2(r_3 - r) + v_3(r - r_2)](r_3 - r_2)^{-1} & \text{if} \quad r_2 \le r < r_3 \\ v_3(r_3/r)^{0.4} & \text{if} \quad r_3 \le r < \infty, \end{cases} \tag{17}$$

where $r_1 = 10$ km, $r_2 = 50$ km, $r_3 = 60$ km, $v_1 = 70$ m s^{-1}, $v_2 = v_1(r_1/r_2)^{0.5}$, and $v_3 = 50$ m s^{-1}. Here we note that $\zeta^2 > S_1^2 + S_2^2$ in the regions $0 \le r < r_1$ and $r_2 < r < r_3$ because $dv_\theta/dr > 0$ and $v_\theta > 0$ in these regions. However, $S_1^2 + S_2^2 > \zeta^2$ in the regions $r_1 < r < r_2$ and $r_3 < r < \infty$. Using (17) in (11), the filamentation time can be expressed as

$$\tau_{\text{fil}}(r) = \begin{cases} (0.5)^{-1/2}(r_1/v_1)(r/r_1)^{1.5} & \text{if} \quad r_1 < r < r_2 \\ (0.4)^{-1/2}(r_3/v_3)(r/r_3)^{1.4} & \text{if} \quad r_3 < r < \infty. \end{cases} \tag{18}$$

Both (17) and (18) are plotted in Fig. 3. In the region between 10 and 43 km and the region just outside 60 km the filamentation times are less than 30 min. The effect of the secondary eyewall region is to provide a haven of rotation-dominated flow and to effectively reset the filamentation time to a lower value just outside this haven.

Radial profiles of filamentation time computed from actual hurricane data are not as smooth as the idealized dashed curves in Figs. 2 and 3. Noisier profiles are given in Figs. 1c,f, which show $\tau_{\text{fil}}(r)$ computed from the Hurricane Gilbert tangential wind data on 13 and 14 September 1988. In regard to Figs. 1c,f, it is worth noting that filamentation times just outside the radius of maximum winds have changed little even though an eyewall replacement cycle has apparently commenced. How-

ever, as the eyewall replacement cycle proceeds, the PV sheet near 10-km radius collapses, and the inner tangential wind maximum and its attendant rapid filamentation zone are lost, which leaves the region between 15 and 50 km more favorable for deep convection.

Although we have presented the concept of rapid filamentation zones in terms of the vorticity equation, the concept is more general. For example, if q is a scalar field obeying

$$\frac{Dq}{Dt} = \dot{q}, \tag{19}$$

then the equation governing the horizontal derivatives of q is

$$\frac{D}{Dt}\begin{pmatrix} q_x + iq_y \\ q_x - iq_y \end{pmatrix} = \begin{pmatrix} \frac{1}{2}i\zeta & -\frac{1}{2}(S_1 + iS_2) \\ -\frac{1}{2}(S_1 - iS_2) & -\frac{1}{2}i\zeta \end{pmatrix} \times \begin{pmatrix} q_x + iq_y \\ q_x - iq_y \end{pmatrix} + \begin{pmatrix} \dot{q}_x + i\dot{q}_y \\ \dot{q}_x - i\dot{q}_y \end{pmatrix}, \tag{20}$$

where $\dot{q}$ represents the material source term. For simplicity, vertical advective effects are neglected. In the context of a full-physics model, q could represent the specific entropy of moist air (alternatively, the equivalent potential temperature), the mixing ratio of total airborne moisture (i.e., the sum of the mixing ratios of water vapor and airborne condensate), the mixing ratio of precipitation, or even the moist PV (Schubert et al. 2001; Schubert 2004). Since the 2×2 matrix in (20) is identical to the one in (3), all these fields' gradients should behave in a similar way as vorticity gradients within the rapid filamentation zone.

Before presenting numerical results in sections 3–5, it should be pointed out that these experiments will display many of the characteristics of 2D turbulence, in particular the selective decay of enstrophy and total strain. To help understand this point, we recall that two quadratic integral properties associated with (1) on a periodic domain are the energy and enstrophy relations $d\mathcal{E}/dt = -2\nu\mathcal{Z}$ and $d\mathcal{Z}/dt = -2\nu\mathcal{P}$, where $\mathcal{E} = \iint \tfrac{1}{2}\nabla\psi \cdot \nabla\psi \, dx\, dy$ is the energy, $\mathcal{Z} = \iint \tfrac{1}{2}\zeta^2 \, dx\, dy$ is the enstrophy, and $\mathcal{P} = \iint \tfrac{1}{2}\nabla\zeta \cdot \nabla\zeta \, dx\, dy$ is the palinstrophy, a measure of the overall vorticity gradient. During the advective rearrangement of vorticity, $\mathcal{P}$ can rapidly increase, and for sufficiently small values of ν, $\mathcal{P}$ can surge to values much larger than its initial value. During the period of heightened $\mathcal{P}$, $\mathcal{Z}$ decays rapidly compared to $\mathcal{E}$, whose rate of decay becomes smaller as $\mathcal{Z}$ decreases. In this way, $\mathcal{Z}$ is selectively decayed over $\mathcal{E}$. This is the essence of the selective decay hypothesis. Since $S_1^2 + S_2^2 - \zeta^2 = -4\partial(u, v)/\partial(x, y)$, integration over the domain yields $\iint \tfrac{1}{2}(S_1^2 + S_2^2)\, dx\, dy = \iint \tfrac{1}{2}\zeta^2 dxdy$, so that the total rate of strain $\iint \tfrac{1}{2}(S_1^2 + S_2^2)\, dx\, dy$, like the enstrophy, is selectively decayed.

3. Filamentation by tropical storms and category 1–5 hurricanes

To demonstrate the evolution of vorticity patches around a strong vortex, we now perform numerical integrations of (1) and (2). The solutions are obtained with a double Fourier pseudospectral model containing 1024×1024 equally spaced collocation points on a doubly periodic domain of size 600 km $\times$ 600 km. The model is run with a dealiased calculation of the quadratic nonlinear terms in (1), resulting in 340×340 Fourier modes. The wavelength of the highest Fourier mode is 1.76 km. Time integration is accomplished via the standard fourth-order Runge–Kutta scheme, with a time step of 5 s. The value of viscosity in (1) is $\nu = 20$ $\mathrm{m^2\,s^{-1}}$. This yields a $1/e$ damping time of 1.1 h for all modes having total wavenumber 340.

The initial condition consists of a circular patch of high vorticity embedded within a stirred vorticity field biased toward cyclonic vorticity. The precise mathematical form of the initial condition is

$$\zeta(x, y, 0) = \zeta_0 + \frac{\Gamma}{\pi b^2} e^{-r^2/b^2} + \zeta_{\mathrm{turb}}(x, y) \times \begin{cases} 1, & 0 \le r < r_1 \\ S\left(\dfrac{r - r_1}{r_2 - r_1}\right), & r_1 \le r < r_2 \\ 0, & r_2 \le r \end{cases}, \tag{21}$$

where $r = (x^2 + y^2)^{1/2}$. With periodic boundary conditions, zero net circulation for the entire domain is desired, yet the two final terms on the right-hand side of (21) yield nonzero circulation. Therefore, ζ_0 in (21) is not a specified constant and it is obtained from the circulation constraint $\iint \zeta(x, y, 0)\, dxdy = 0$. The second term on the right-hand side of (21) is the term for the Gaussian vortex. Here, the constant Γ controls the amplitude of the Gaussian vortex and the constant parameter b governs the shape of the Gaussian vortex profile with respect to r. Finally, the last term represents the stirred field of vorticity; $S(s) = 1 - 3s^2 + 2s^3$ is the basic cubic Hermite shape function satisfying $S(0) = 1$, $S(1) = 0$, $S'(0) = S'(1) = 0$. $S(s)$, and the constants r_1 and r_2

control the size of the stirred vorticity disk. Here, S smoothly damps the turbulent vorticity amplitudes to zero between r_1 and r_2. The surrounding turbulent vorticity field is given by

$$\zeta_{\text{turb}}(x, y) = \sum_{k=-k_{\max}}^{k_{\max}} \sum_{\ell=-\ell_{\max}}^{\ell_{\max}} \zeta_{k,\ell} e^{i(2\pi/L)(kx+\ell y)}. \quad (22)$$

Here, L is the domain size, $\zeta_{0,0}$ is a specified constant that determines the cyclonic bias of the surrounding turbulent vorticity field, and

$$\zeta_{k,\ell} = \hat{\zeta} e^{iR_{k,\ell}} \begin{cases} 0, & 0 \le \kappa < \kappa_1 \\ S\left(\dfrac{\kappa_2 - \kappa}{\kappa_2 - \kappa_1}\right), & \kappa_1 \le \kappa < \kappa_2 \\ 1, & \kappa_2 \le \kappa < \kappa_3 \\ S\left(\dfrac{\kappa - \kappa_3}{\kappa_4 - \kappa_3}\right), & \kappa_3 \le \kappa < \kappa_4 \\ 0, & \kappa_4 \le \kappa \end{cases}, \quad (23)$$

with $\kappa = (k^2 + \ell^2)^{1/2}$ the total wavenumber, $\hat{\zeta}$ the amplitude of the turbulent vorticity fluctuations, and $R_{k,\ell}$ random numbers between zero and 2π. The constant specified wavenumbers κ_1, κ_2, κ_3, and κ_4 determine the spatial scales of the random vorticity elements in the stirred vorticity field.

In the current experiments, we specify $\Gamma = 2\pi(7.5 \times 10^5)$ m^2 s^{-1}, $r_1 = 120$ km, $r_2 = 130$ km, $\kappa_1 = 0$, $\kappa_2 = 15$, $\kappa_3 = 30$, $\kappa_4 = 45$, $\zeta_{0,0} = 1 \times 10^{-4}$ s^{-1}, $\hat{\zeta} = 1.5 \times 10^{-5}$ s^{-1}, and run six experiments for the six values of b given in Fig. 2. Associated with the total wavenumber κ is a horizontal scale 600 km/κ, so that the range of turbulence wavenumbers $0 \le \kappa \le 45$ corresponds to horizontal scales greater than 13 km. Most of the random vorticity elements have a scale between 20 and 40 km. These random elements can be viewed as the result of vorticity generation by small groups of irregularly spaced cumulonimbus clouds. Tropical Rainfall Measuring Mission (TRMM) data show such scales are common in tropical convection near intensifying storms. Figure 4 shows the spatial distribution of the stirred vorticity field [i.e., the last term on the right-hand side of (21)].

To illustrate the effects of rapid filamentation, Fig. 5 shows the vorticity distribution at $t = 30$ min for each of the experiments described above. Regions of enhanced vorticity in Fig. 4 undergo merger events and simultaneously demonstrate filamentation. In all the panels in Fig. 5, the distribution of turbulent vorticity elements is nearly identical at radii greater than 40 km. These similarities result from similar advecting tangential winds,

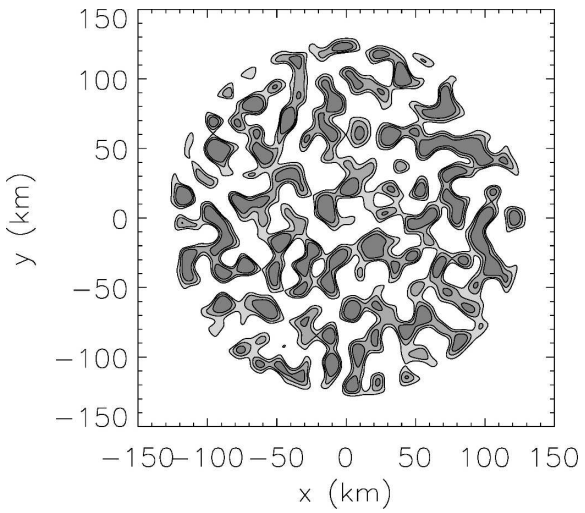

FIG. 4. Contour plot of the turbulent part of the initial vorticity field [i.e., the last term on the rhs of (21)]. The model domain encompasses 600 km × 600 km but only the inner 300 km × 300 km is displayed. Vorticity contours are at 1.0×10^{-4}, 5.0×10^{-4}, and 10.0×10^{-4} s^{-1}, with the darkest shading representing the highest values of vorticity.

as observed in Fig. 2a, at radii larger than 40 km. On the other hand, it is evident that at smaller radii, the stronger vortices deform the turbulent vorticity more efficiently, leading to even more rapid filamentation. Clearly, the filaments around the category 5 vortex are much finer than those forming around the tropical storm. As illustrated in Fig. 2, stronger Gaussian monopoles, which possess larger radial gradients of tangential wind, yield higher values of strain. In the nondivergent barotropic framework, this is the physical mechanism leading to the development of a moat around the vortex core. If the central vortex is strong enough, continued evolution of the vorticity field eventually leads to the formation of a weakly positive vorticity ring outside of a smooth, axisymmetric moat of slightly negative vorticity.

4. Evolution of rapid filamentation zones during a binary vortex interaction

An interesting example of vortex interaction is the evolution of two initially circular, vortex patches in close proximity. One patch with small area, but large vorticity can be considered the TC core. The other patch containing larger area, but much weaker vorticity can be considered a weaker, nearby storm or simply enhanced vorticity generated in surrounding asymmetric convection. Recently Prieto et al. (2003) and Kuo et al. (2004) ran numerous barotropic model experiments with a range of vortex area ratios, peak vorticity ratios,

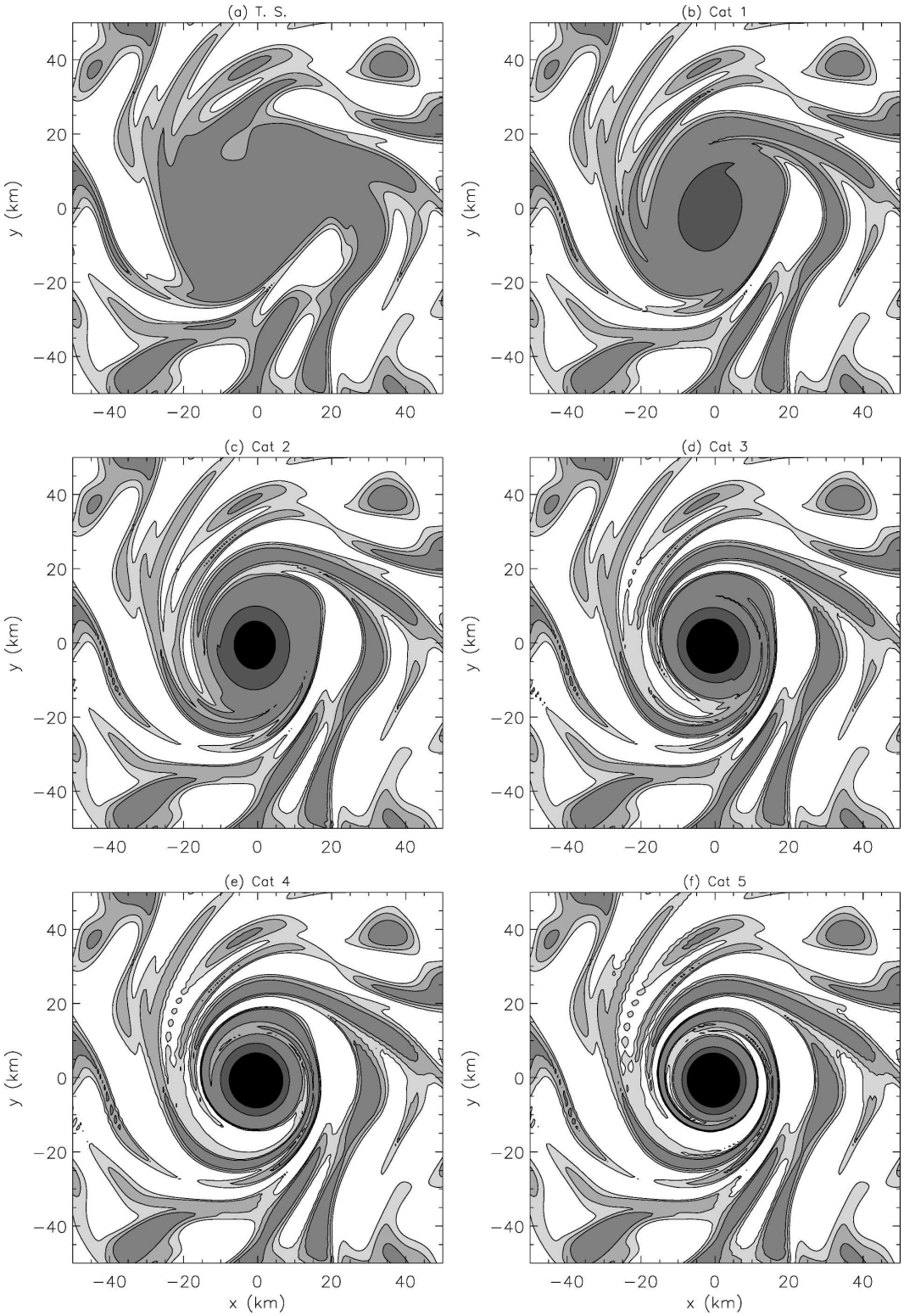

FIG. 5. Barotropic model results at $t = 30$ min for the six Gaussian vortices with a superimposed turbulent field. Vorticity is plotted for (a) $b = 20$ km (tropical storm), (b) $b = 13$ km (category 1 tropical cyclone), (c) $b = 10.2$ km (category 2), (d) $b = 8.5$ km (category 3), (e) $b = 7.4$ km (category 4), and (f) $b = 6.3$ km (category 5). Shaded regions are separated by the vorticity contours 1×10^{-4}, 5×10^{-4}, 10×10^{-4}, 50×10^{-4}, and 100×10^{-4} s^{-1}. The darker shading represents higher values of vorticity. The model domain encompasses 600 km $\times$ 600 km, but only the inner 100 km $\times$ 100 km is displayed.

and separation distances. They classified the resulting interactions using the scheme devised by Dritschel and Waugh (1992). An important conclusion of these papers is that one way to produce a halo of enhanced vorticity around an intense vortex is through a binary interaction in which the weaker vortex is completely strained out. This mode of interaction is most likely to occur when the peak vorticity in the strong vortex is at least 5 times that of the weak vortex (Kuo et al. 2004, Fig. 10).

To understand how rapid filamentation zones evolve during such vortex interactions, the experiments depicted in Fig. 6 are performed. In this experiment the domain size is 200 km × 200 km (but only the inner 100 km × 100 km is displayed) and the value of viscosity is set to $\nu = 6.5\ \mathrm{m^2\ s^{-1}}$. The initial condition consists of two circular vortex patches with sharp edges. Initially, the small patch has a nearly uniform vorticity equal to $1.5 \times 10^{-2}\ \mathrm{s^{-1}}$) and a radius of 10 km. Meanwhile, the larger patch has an almost uniform vorticity equal to $2.5 \times 10^{-3}\ \mathrm{s^{-1}}$ and a radius of 30 km. The distance between the vorticity centers is 50 km. As shown in Fig. 6a, the large, weak vortex has been completely strained out after 3 h. At 6 h (not shown), the tightly wound portion of the spiral acquires an irregular character while the outer portion becomes very thin. By 12 h, the central core of high vorticity is surrounded by a moat of low vorticity, which in turn is surrounded by a halo of enhanced vorticity from the original weak vortex. Outside the halo is a region of irregular vorticity, associated with dissipating thin spiral bands. This outer region is qualitatively similar to the irregular region outside 65-km radius in the Hurricane Gilbert azimuthal wind profile shown in Fig. 1e.

The corresponding distributions of filamentation time, computed from (7), are shown in Fig. 6b. The white areas are regions where the flow is rotation-dominated. There are five shades of gray, indicating filamentation times $\tau_{\mathrm{fil}} < 7.5$ min (black region), $7.5 < \tau_{\mathrm{fil}} < 15$ min, $15 < \tau_{\mathrm{fil}} < 30$ min, $30 < \tau_{\mathrm{fil}} < 45$ min, $45 < \tau_{\mathrm{fil}}$ (lightest gray region). The three darkest regions indicate the rapid filamentation zone. At 12 h, there are alternating layers of rotation-dominated and strain-dominated flow with a rapid filamentation zone approximately 15 km wide immediately outside the central core of high vorticity. Such layering seems to be a robust feature of the interaction of a small intense vortex with a large region of relatively weak vorticity.

Can a strong vortex imposed upon a stirred field of vorticity lead to a halo of vorticity similar to those formed in the experiments of Kuo et al. (2004)? Let us consider the experiments described in section 3. In this case however, the second Gaussian term in (21) is replaced with $\zeta_{\max} S[(r - r_3)/(r_4 - r_3)]$, where $S(x)$ is the basic cubic Hermite shape function defined earlier, and r_3 and r_4 are defined to approximate an intense TC. This structure is approximately a Rankine vortex. Choosing $\zeta_{\max} = 6.5 \times 10^{-3}\ \mathrm{s^{-1}}$, the central vortex approximates a category 5 hurricane with maximum tangential winds of $75.5\ \mathrm{m\ s^{-1}}$ near $r = 25$ km. The simulation is carried out as before, except this time, it continues for 48 h.

The results of this experiment are illustrated in Fig. 7. As indicated in Fig. 7a, the strong vortex dominates the field of turbulent vorticity and preferentially filaments the vorticity closer to the core at 9 h, clearing much of the vorticity within a 30-km-wide annulus surrounding the core. Vorticity patches in the far field are less dominated by the core's motions, and therefore, these patches have pronounced interaction with neighboring vorticity patches. Nevertheless, as the far field is still strain-dominated on average, after 45 h the outer vorticity patches have strained out, leaving a fairly axisymmetric vorticity distribution about the storm's center. Smaller filamentation times near the core, as presented in Fig. 7b, eliminate vorticity around the core. A halo of weak vorticity begins at a radius of about 70 km from the center. The magnitude of this vorticity halo is an order of magnitude less than the halo resulting from the binary interaction experiment. Initially, the magnitude of the central core is only one order greater than the surrounding stirred vorticity, but after about 45 h, the difference is two orders of magnitude. Because of the del-squared diffusion term in the vorticity equation, diffusion acts aggressively on the scales of the small vorticity elements. At the same time, the larger and uniform vorticity patch observed in the binary vortex experiment remains relatively protected from diffusion.

5. Evolution of rapid filamentation zones during mesovortex formation

Observed flows in intensifying TCs sometimes resemble an idealized circular flow with a thin annular ring of enhanced vorticity (Kossin and Eastin 2001). These flows tend to be highly unstable and, in certain circumstances, can break down into a number of mesovortices (Kossin and Schubert 2001, hereafter KS01; Montgomery et al. 2002; Kossin et al. 2002). The experiments presented in Figs. 8 and 9 provide some insight into the evolution of rapid filamentation zones during mesovortex formation. The initial condition for these two experiments is $\zeta(r, \phi, 0) = \bar{\zeta}(r) + \zeta'(r, \phi)$, where $\zeta'(r, \phi)$ is a small perturbation of the axisymmetric vorticity field

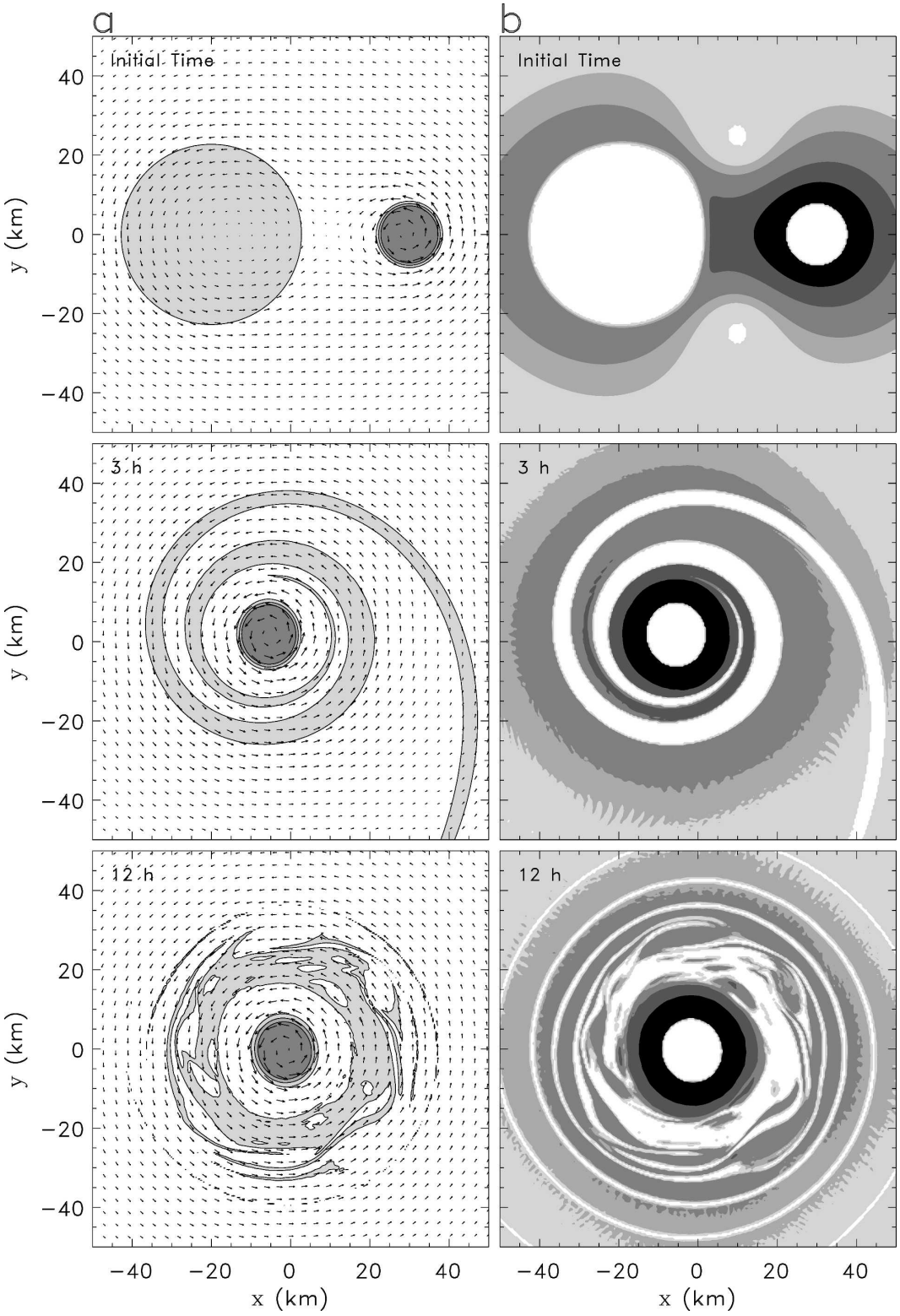

FIG. 6. (a) Vorticity contour plots and horizontal wind vectors for the binary interaction experiment are shown in the left three panels. The contours are 10×10^{-4}, 50×10^{-4}, and 100×10^{-4} s^{-1}, with darker shading denoting higher vorticity. (b) Corresponding filamentation times for the panels to the left. The shaded regions are separated by filamentation times of 45, 30, 15, and 7.5 min, with darker shadings representing the smallest times. The model domain is 200 km × 200 km but only the inner 100 km × 100 km is plotted.

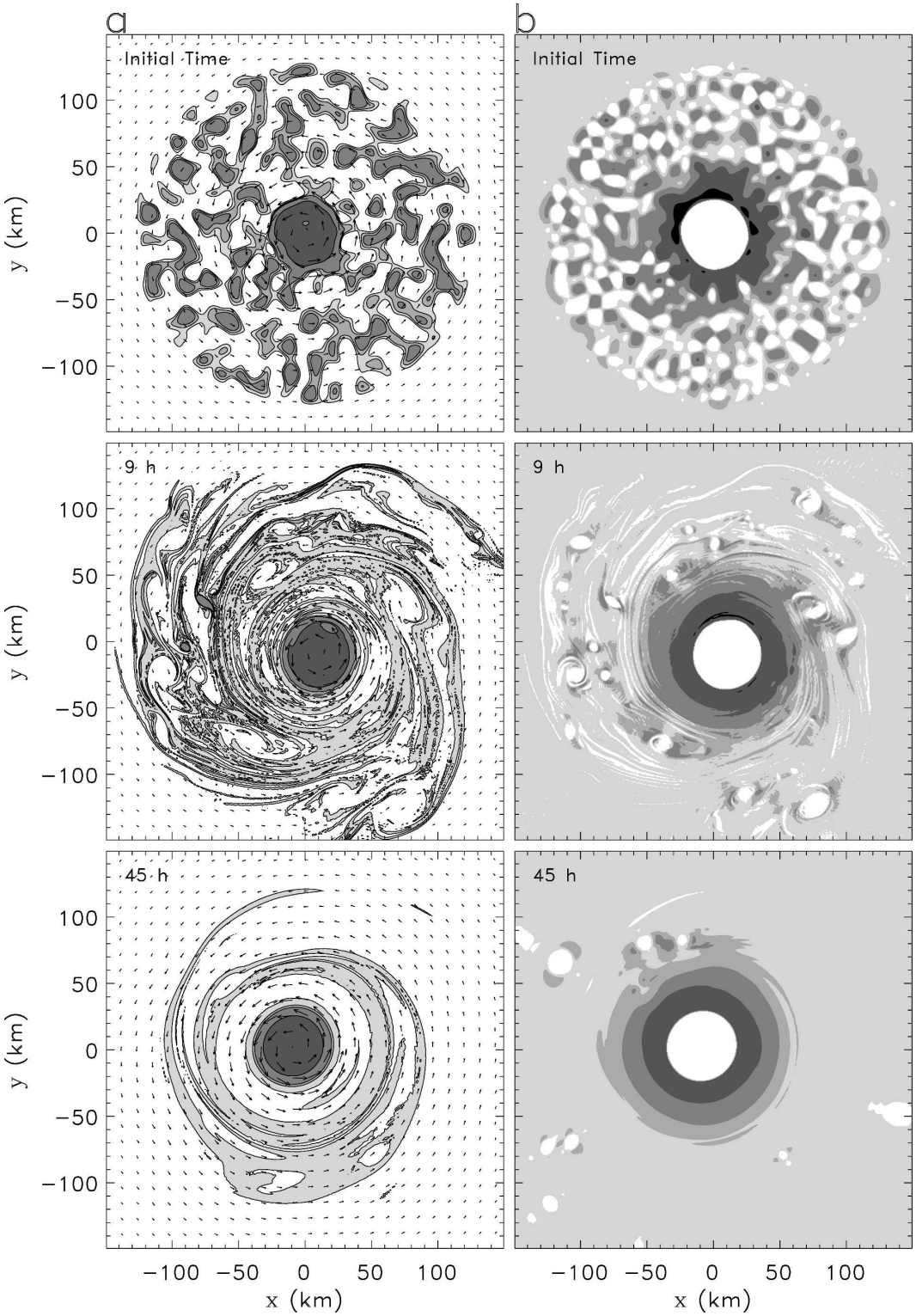

FIG. 7. (a) Vorticity contour plots and horizontal wind vectors. The contours are 1×10^{-4}, 5×10^{-4}, 10×10^{-4}, and 50×10^{-4} s^{-1}. Darker shading denotes higher vorticity. (b) Corresponding filamentation times for the panels to the left. Shaded regions are separated by filamentation times of 45, 30, 15, and 7.5 min, with darker shadings representing the smallest times. The model domain is 600 km × 600 km, but only the inner 300 km × 300 km is plotted.

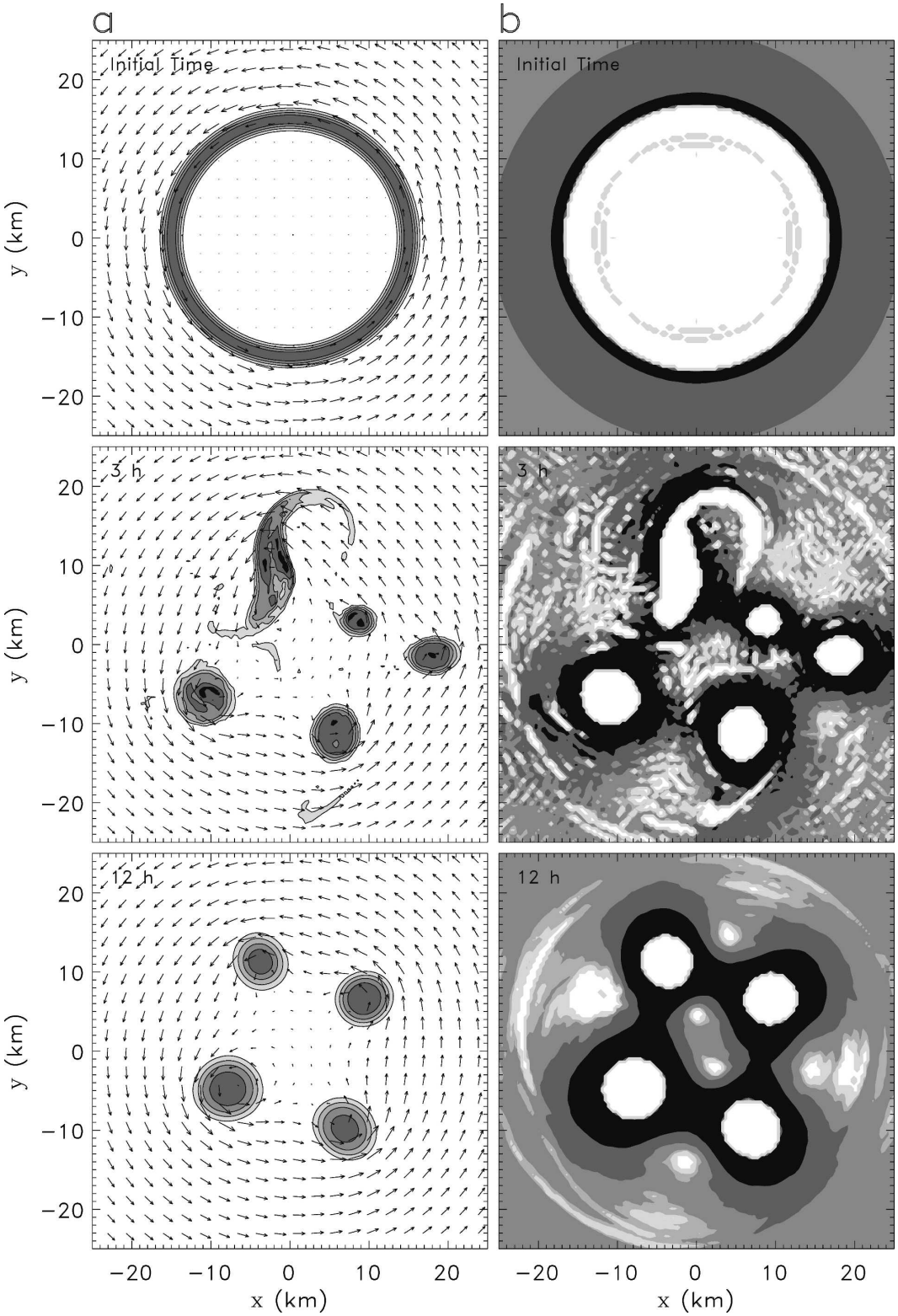

FIG. 8. (a) Vorticity contour plots and horizontal wind vectors for the first thin annular vorticity ring experiment. The contours begin at 5×10^{-3} s^{-1} and are incremented by 5×10^{-3} s^{-1}. Darker shading denotes higher vorticity. (b) Corresponding filamentation times for the panels to the left. Shaded regions are separated by filamentation times of 45, 30, 15, and 7.5 min, with darker shadings representing the smallest times. The model domain is 200 km $\times$ 200 km but only the inner 50 km $\times$ 50 km is plotted.

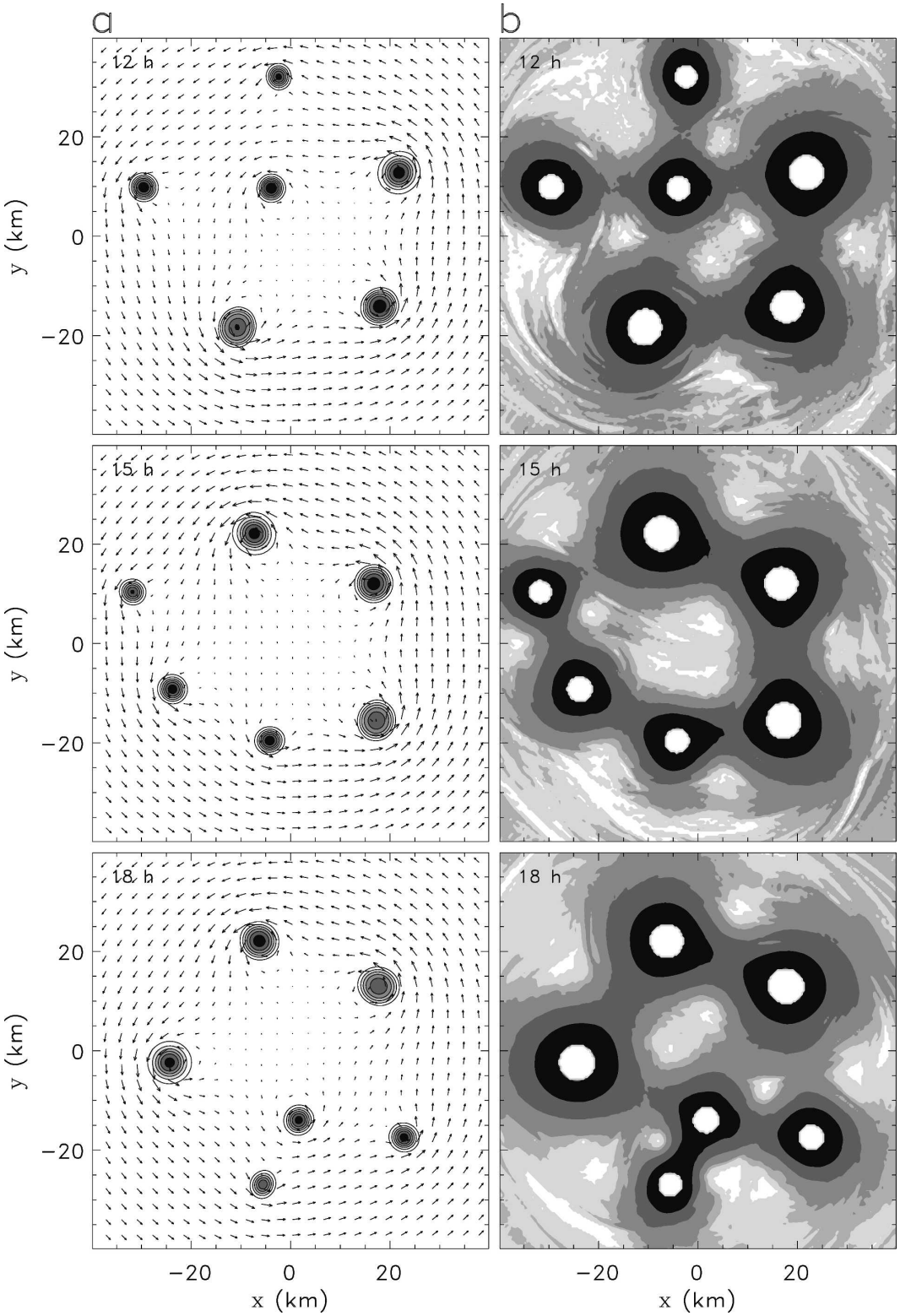

FIG. 9. (a) Vorticity contour plots and horizontal wind vectors for the second thin annular vorticity ring experiment. The contours begin at 5×10^{-3} s^{-1} and are incremented by 5×10^{-3} s^{-1}. Darker shading denotes higher vorticity. (b) Corresponding filamentation times for the panels to the left. Shaded regions are separated by filamentation times of 45, 30, 15, and 7.5 min, with darker shadings representing the smallest times. The model domain is 200 km × 200 km but only the inner 80 km × 80 km is plotted.

$$\bar{\zeta}(r) = \begin{cases} \zeta_1 & 0 < r < r_1, \\ \zeta_1 S[(r - r_1)/(r_2 - r_1)] + \zeta_2 S[(r_2 - r)/(r_2 - r_1)] & r_1 \le r < r_2, \\ \zeta_2 S[(r - r_2)/(r_3 - r_2)] + \zeta_1 S[(r_3 - r)/(r_3 - r_2)] & r_2 \le r < r_3, \\ \zeta_1 & r_3 \le r < r_4, \\ \zeta_1 S[(r - r_4)/(r_5 - r_4)] + \zeta_3 S[(r_5 - r)/(r_5 - r_4)] & r_4 \le r < r_5, \\ \zeta_3 & r_5 \le r < \infty, \end{cases} \tag{24}$$

where r_1, r_2, r_3, r_4, r_5, ζ_1, ζ_2, and ζ_3 are independently specified quantities, and $S(s)$ is the same basic cubic Hermite shape function used in (21). This initial condition is identical to that imposed in experiments 1 and 6 of KS01. In the present simulations, a slightly different initial random noise perturbation $\zeta'(r, \phi)$ is chosen, but, as in KS01, it is also 1% of the local vorticity. A comparison of the present results with KS01 reveals the sensitivity to subtle differences in the initial conditions—an expected result considering the chaotic behavior of this simple nonlinear system. For the results shown in Figs. 8 and 9, Eqs. (1) and (2) are integrated with 512 × 512 collocation points on a 200 km × 200 km domain. The viscosity is chosen as $\nu = 5\ \mathrm{m^2\ s^{-1}}$ and the time step is 5 s.

For the experiment shown in Fig. 8, $(r_1, r_2, r_3, r_4, r_5) = (13, 15, 17, 35, 45)$ km and $(\zeta_1, \zeta_2, \zeta_3) = (1.02, 248.52, -1.48) \times 10^{-4}\ \mathrm{s^{-1}}$, which yield a vortex with maximum tangential winds of 45 m s^{-1}, at $r = 17$ km. Figure 8a depicts vorticity and the associated wind field. The thin annulus quickly experiences exponential growth of small initial perturbations, resulting in numerous mesovortices. Many have merged by $t = 3$ h. Eventually, a quasi-stable configuration of four vortices materializes. The interesting features include the persistent general cyclonic flow surrounding an interior region of relatively calm winds. This flow steers the mesovortices in a cyclonic orbit. Each mesovortex induces an asymmetric circulation about itself.

Given the particular wind distributions associated with the mesovortex configurations, it is valuable to study where rapid filamentation occurs. Figure 8b displays filamentation times for the corresponding plots on the left-hand side. The contouring scheme is described with more detail in section 4. Gibbs phenomena are somewhat noticeable in these experiments, especially apparent in the τ_{fil} field. Rapid filamentation always occurs on the outside regions of all areas of higher vorticity. In this case, it would be difficult to maintain weaker vorticity and convective clouds around each mesovortex perimeter.

For the second experiment, shown in Fig. 9, $(r_1, r_2, r_3, r_4, r_5) = (30, 30.5, 32, 40, 45)$ km and $(\zeta_1, \zeta_2, \zeta_3) = (1.02, 395.0, -1.48) \times 10^{-4}\ \mathrm{s^{-1}}$. These choices result in an initial maximum wind of 74 m s^{-1} around $r = 33$ km. In Fig. 9a, vorticity and wind fields are plotted every 3 h starting at 12 h As in KS01, six mesovortices maintain themselves in an alternating wavenumber-5 or -6 pattern as one vortex migrates in and out of the center. As before, winds are relatively calm in the center and stronger and more cyclonic on the outskirts. Each mesovortex also induces its own asymmetric circulation about itself. In this case, however, when one vortex periodically migrates into the interior region, an asymmetric pattern in the wind field appears and stronger winds are carried into the eye.

Figure 9b shows filamentation times corresponding with Fig. 9a. Again, each mesovortex is surrounded by a region of rapid filamentation. Elsewhere, the filamentation time is much longer. In nature, if 2D nondivergent barotropic dynamics were the only physics at work, given sufficiently thin rings of vorticity, similar vorticity structures would be found in TC inner cores.

As a point of interest, Fig. 10 provides a Defense Meteorological Satellite Program (DMSP) visible image of the inner core of Hurricane Isabel at 1315 UTC 12 September 2003 (Kossin and Schubert 2004). At the time of this image, the maximum sustained winds in the eyewall were 70 m s^{-1} and the eye was approximately 65 km in diameter. This image is suggestive that vortex crystal patterns similar to Fig. 9 may emerge in nature. A particularly interesting feature of this image is the hub cloud (Simpson and Starrett 1955) at the center of the eye. This feature resembles the central mesovortex in the upper left panel of Fig. 9. Further analysis is needed to determine how the mesovortex behavior differs from the 2D nondivergent barotropic mesovortices.

6. Concluding remarks

We defined a rapid filamentation zone as the part of the strain-dominated flow region in which $\tau_{\mathrm{fil}} < \tau_{\mathrm{conv}}$, where τ_{fil} is based on the Okubo–Weiss eigenvalues describing the evolution of tracer gradients, and where the moist convective overturning time is $\tau_{\mathrm{conv}} = 30$ min. Rapid filamentation zones are less likely in weak tropical disturbances, but in symmetric hurricanes they tend

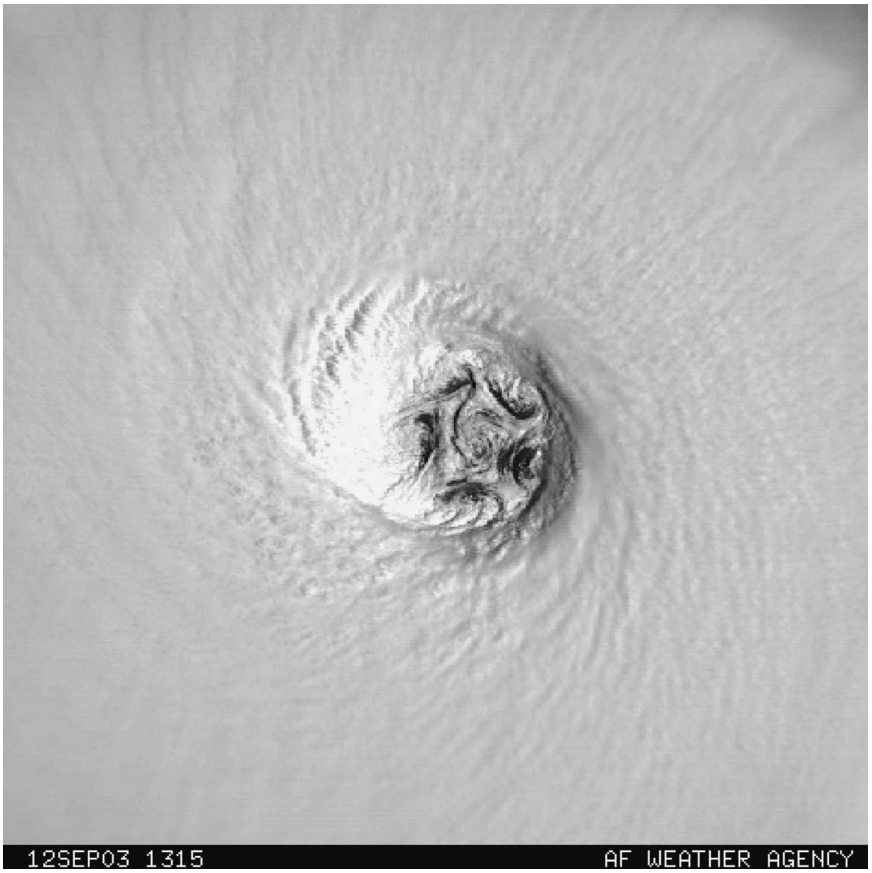

FIG. 10. DMSP (*F15*) visible image of Hurricane Isabel on 1315 UTC 12 Sep 2003. At 0900 UTC 12 Sep, the MSLP was 936 hPa. At 1500 UTC 12 Sep, the MSLP was 924 hPa. The approximate dimensions of the figure are 200 km × 200 km.

to occupy an annular region 20–30 km wide just outside the radius of maximum wind. In symmetric, intense hurricanes with secondary eyewalls, another (but narrower) rapid filamentation zone can occur just outside the secondary wind maximum. If mesovortices form and the storm becomes asymmetric, the rapid filamentation zone can extend into the eye, where strain rates can be very large even though the flow is weak (bottom panels of Fig. 8). In the binary interactions, it appears that the rapid filamentation zone outside of a more intense vortex can influence the development of a moat.

It was hypothesized that both subsidence and rapid filamentation are important to the formation and maintenance of a moat. Although an evaluation of the relative importance of these two effects is beyond the simple barotropic arguments presented here, it is easy to envision how they might work together to produce a moat. As a tropical storm evolves into a young hurricane, with convection fairly uniform outside the eye, the filamentation time outside the radius of maximum wind begins to decrease. Convective activity begins to decrease in 20–30-km-wide annular ring outside the radius of maximum wind and increases near the radius of maximum wind, thus concentrating the upward motion and latent heat release at smaller radii while suppressing upward motion in the annular ring. The large latent heat release near the radius of maximum wind builds the PV there to high values. The values of PV and vorticity are relatively low just outside this evolving wall of high PV, so that the azimuthal wind has the form $v \sim r^{-1}$, which is favorable for even smaller filamentation times and further suppression of convection. Thus, in this scenario, there is a positive feedback process whereby convection shifts inward, a wall of high PV develops, and a strain-dominated subsiding moat develops between concentric eyewalls. Research with full-physics models is required for a more complete understanding of such feedback processes. An interesting starting point would be 3D simulations of deep, moist convective clouds embedded in a background flow with vertical motion and large horizontal strain.

In closing, it should be pointed out there have been recent efforts to improve the Okubo–Weiss criterion by relaxing its assumption that velocity gradients are slowly varying following a fluid parcel. In particular, Hua and Klein (1998) have proposed an improved criterion, from which a more precise definition of τ_{fil} is easily obtained. We have also computed this more accurate τ_{fil} but found that, for the examples presented in this paper, the changes are not dramatic. However, the more accurate argument does produce somewhat larger rapid filamentation zones with smaller values of τ_{fil}, so that the estimates of the size and intensity of rapid filamentation zones given in the figures presented here should be regarded as conservative.

Acknowledgments. We thank Dr. Michael Black, Dr. Mark DeMaria, Dr. Michael Montgomery, Jill Schaefer, Dr. Yuqing Wang, and Dr. Hugh Willoughby for their comments and suggestions. Rick Taft provided dedicated support with the nondivergent barotropic model and helped set up initial conditions for some of the experiments. Comments from two anonymous reviewers also greatly improved the quality of this manuscript. CR, WS, and BM were supported by NASA/CAMEX Grant NAG5-11010 and NASA Grant TCSP/04-0007-0031. JK was supported by NSF Grant ATM-0435694.

REFERENCES

Black, M. L., and H. E. Willoughby, 1992: The concentric eyewall cycle of Hurricane Gilbert. *Mon. Wea. Rev.,* **120,** 947–957.

Brachet, M. E., M. Meneguzzi, H. Politano, and P. L. Sulem, 1988: The dynamics of freely decaying two-dimensional turbulence. *J. Fluid Mech.,* **194,** 333–349.

Dodge, P., R. W. Burpee, and F. D. Marks Jr., 1999: The kinematic structure of a hurricane with sea level pressure less than 900 mb. *Mon. Wea. Rev.,* **127,** 987–1004.

Dritschel, D. G., and D. W. Waugh, 1992: Quantification of the inelastic interaction of unequal vortices in two-dimensional dynamics. *Phys. Fluids A,* **4,** 1737–1744.

Guinn, T. A., and W. H. Schubert, 1993: Hurricane spiral bands. *J. Atmos. Sci.,* **50,** 3380–3403.

Hua, B. L., and P. Klein, 1998: An exact criterion for the stirring properties of nearly two-dimensional turbulence. *Physica D,* **113,** 98–110.

Kossin, J. P., and M. D. Eastin, 2001: Two distinct regimes in the kinematic and thermodynamic structure of the hurricane eye and eyewall. *J. Atmos. Sci.,* **58,** 1079–1090.

——, and W. H. Schubert, 2001: Mesovortices, polygonal flow patterns, and rapid pressure falls in hurricane-like vortices. *J. Atmos. Sci.,* **58,** 2196–2209.

——, and ——, 2004: Mesovortices in Hurricane Isabel. *Bull. Amer. Meteor. Soc.,* **85,** 151–153.

——, ——, and M. T. Montgomery, 2000: Unstable interactions between a hurricane's primary eyewall and a secondary ring of enhanced vorticity. *J. Atmos. Sci.,* **57,** 3893–3917.

——, B. D. McNoldy, and W. H. Schubert, 2002: Vortical swirls in hurricane eye clouds. *Mon. Wea. Rev.,* **130,** 3144–3149.

Kuo, H.-C., L.-Y. Lin, C.-P. Chang, and R. T. Williams, 2004: The formation of concentric vorticity structures in typhoons. *J. Atmos. Sci.,* **61,** 2722–2734.

Montgomery, M. T., V. A. Vladimirov, and P. V. Denissenko, 2002: An experimental study on hurricane mesovortices. *J. Fluid Mech.,* **471,** 1–32.

Okubo, K., 1970: Horizontal dispersion of floatable particles in the vicinity of velocity singularities such as convergences. *Deep-Sea Res.,* **17,** 445–454.

Prieto, R., B. D. McNoldy, S. R. Fulton, and W. H. Schubert, 2003: A classification of binary tropical-cyclone-like vortex interactions. *Mon. Wea. Rev.,* **131,** 2656–2666.

Samsury, C. E., and E. J. Zipser, 1995: Secondary wind maxima in hurricanes: Airflow and relationship to rainbands. *Mon. Wea. Rev.,* **123,** 3502–3517.

Schubert, W. H., 2004: A generalization of Ertel's potential vorticity to a cloudy, precipitating atmosphere. *Meteor. Z.,* **13,** 465–471.

——, S. A. Hausman, M. Garcia, K. V. Ooyama, and H.-C. Kuo, 2001: Potential vorticity in a moist atmosphere. *J. Atmos. Sci.,* **58,** 3148–3157.

Shapiro, L. J., and M. T. Montgomery, 1993: A three-dimensional balance theory for rapidly rotating vortices. *J. Atmos. Sci.,* **50,** 3322–3335.

Simpson, R. H., and L. G. Starrett, 1955: Further studies of hurricane structure by aircraft reconnaissance. *Bull. Amer. Meteor. Soc.,* **36,** 459–468.

Weiss, J., 1991: The dynamics of enstrophy transfer in two-dimensional hydrodynamics. *Physica D,* **48,** 273–294.